

High capacity Li/Ni rich Ni-Ti-Mo oxide cathode for Li-ion batteries

Jianan Xu^a, Ganguli Babu^{a,*}, Keiko Kato^a, Francisco C. Robles Hernández^{a,b}, Anand B. Puthirath^a, Alexander Britz^{c,d}, Dennis Nordlund^e, Sami Sainio^e, Uwe Bergmann^c, Pulickel M. Ajayan^{a,*}

^a Department of Materials Science and NanoEngineering, Rice University, Houston, TX 77005, USA

^b Mechanical Engineering Technology, University of Houston, Houston, TX, USA

^c Stanford PULSE Institute, SLAC National Accelerator Laboratory, Menlo Park, CA 94025, USA

^d Linac Coherent Light Source, SLAC National Accelerator Laboratory, Menlo Park, CA 94025, USA

^e Stanford Synchrotron Radiation Lightsources, SLAC National Accelerator Laboratory, Menlo Park, CA 94025, United States

ARTICLE INFO

Keywords:

Li-ion battery
Li excess cathodes
Order-disorder materials
Oxygen redox activity
X-ray absorption spectroscopy

ABSTRACT

With the rising cost and insufficient supply of cobalt, the thrust for cobalt-free cathode materials with the high specific capacity to build Li-ion batteries has increased significantly. Using nickel as the prime electrochemical active species, we have synthesized a new-class of materials with the combination of ordered and disordered phases. To obtain high capacity and electrical charge neutrality, stoichiometry of cations designed in a way that it forms Li/Ni rich Ni-Ti-Mo oxide materials. In addition to conventional capacity from redox activity of transition metals, partially reversible oxygen redox reaction also contributes to electrochemical activity and thus results in unusual high capacity. The resultant cathode materials of $\text{LiNi}_{0.5}\text{Ti}_{0.5}\text{O}_2\text{-(Li}_4\text{MoO}_5\text{)}_{0.8}$ and LiNiO_2 mixture phases reach the specific capacity of 240 mAh/g. Detailed soft X-ray absorption spectroscopy and electron microscopy are used to reveal the crystal phases in this system and trace changes in the $\text{Ni}^{2+}/\text{Ni}^{4+}$ redox couple during charge-discharge processes. Such comprehensive analysis of ordered-disordered oxides suggesting potentiality to develop high-capacity cobalt-free cathodes.

1. Introduction

To accelerate the process of replacing fossil fuels with sustainable energy, Li-ion batteries are prime contenders as they store the electricity produced from intermittent renewable energy sources. These are power sources for prevailing portable electronics and potentially pervasive electric vehicles to combat human-induced climate change or global warming. Nevertheless, the energy storage capacity of currently used cathode materials like layered LiCoO_2 (140 mAh/g), $\text{LiNi}_{1/3}\text{Mn}_{1/3}\text{Co}_{1/3}\text{O}_2$ (180 mAh/g) and olivine LiFePO_4 (170 mAh/g) severely limit the energy density [1–3]. Moreover, due to the expensive and scarce availability of widely used cobalt based cathodes, searching for Co-free Li-ion batteries with higher energy density is urgent. Recently, cathode materials with excess lithium in their stoichiometry gain tremendous attention for their capability to deliver high specific capacity around 200–300 mAh/g [4–7]. The combination of classical cationic and anionic redox reactions which transforms the oxygen ion to peroxo-like species results in such incredibly high capacity [8–14].

There have been efforts to access reversible oxygen redox reaction that may be triggered by the so-called “metal-driven reductive coupling mechanism” based on proper band overlap between the metal-oxygen

anti-bonding band (MO^*) and non-bonding oxygen band ($\text{O}(2p)$) as well as strong metal-oxygen covalency bond (M-O) [15–17]. Several structures such as layered Li_2MnO_3 , Li_2RuO_3 and Li_3IrO_4 , [15,18,19] tridimensional $\beta\text{-Li}_2\text{IrO}_3$, and rock salt disordered $\text{Li}_{1.2}\text{Ni}_{0.333}\text{Ti}_{0.333}\text{Mo}_{0.133}\text{O}_2$ [20,21] have been reported in this regard. However, at this moment, it is difficult for those Li-excess cathodes to be applicable since either the migration of Mn or the rare and dense properties of Ru and Ir is an intrinsic issue that would cause the transformation of the layered structure to spinel with tremendous capacity degradation, or play as a penalty to gravimetric energy density [15,22]. Concerning rock salt disordered structure, excess lithium would cause a percolation network activated within which Li is able to diffuse through O-TM channels [23]. Therefore, more lithium ions are available when the charge/discharge process occurring that partially accounts for the larger capacity attained.

In this study, we aim to prepare Li/Ni-rich Ni-Ti-Mo oxide with the nominal formula $\text{Li}_{1.14}\text{Ni}_{0.57}\text{Ti}_{0.19}\text{Mo}_{0.10}\text{O}_2$ to reach the higher capacity than the state-of-art layered cathodes by combining cationic and anionic redox reactions. Taking the anionic redox availability and structure stability schemed in the rock-salt disordered work into consideration, the stoichiometry of Li is deliberately chosen to be 1.14. To

* Corresponding authors.

E-mail addresses: babu.ganguli@rice.edu (G. Babu), ajayan@rice.edu (P.M. Ajayan).

keep the main electrochemically active species, namely, nickel in +2 valence rather in +3, which for the purpose of elevating the capacity part delivered by transition metal ions, we have chosen molybdenum with highest oxidation state and adjusted the ratio between transition metals accordingly. Moreover, titanium is selected to form $\text{LiNi}_{0.5}\text{Ti}_{0.5}\text{O}_2$ where the characteristic Li-O-Li configuration in the crystal structure is in favor of triggering anionic redox according to the above mentioned research as well. The theoretical calculation suggests that Ni can deliver a specific capacity of 227 mAh/g. Along with the partial capacity contributed from triggered oxygen redox reaction, the proposed electrode is expected to have a much higher specific capacity than a solely Ni-based prediction. However, the synthesis at different temperatures resulted in mixed phases as $\text{LiNi}_{0.5}\text{Ti}_{0.5}\text{O}_2\text{-(Li}_4\text{MoO}_5\text{)}_{0.8}\text{-LiNiO}_2$ at 800 °C and $\text{LiNi}_{0.5}\text{Ti}_{0.5}\text{O}_2\text{-(Li}_4\text{MoO}_5\text{)}_{0.8}\text{-Li}_{0.5}\text{Ni}_{0.5}\text{O}$ at 750 °C. The combination of spectroscopy and microscopy techniques in-conjunction with electrochemical cycling reveal the existence of aforementioned crystal phases and the occurrence of Ni^{2+} to $\text{Ni}^{3+}/\text{Ni}^{4+}$ redox couple and oxygen redox reaction.

2. Experimental section

2.1. Synthesis

CH_3COOLi (Sigma Aldrich, 99.9%), $\text{Ni}_2(\text{NO}_3)_2\cdot 6\text{H}_2\text{O}$ (Sigma Aldrich, 99.9%), TiO_2 (Sigma Aldrich, 99.9%) and $(\text{NH}_4)_6\text{Mo}_7\text{O}_{24}\cdot 4\text{H}_2\text{O}$ (Sigma Aldrich, 99.9%) were used as precursors. At the beginning, aiming for the atomic ratio Li:Ni:Ti:Mo as 1.14:0.57:0.19:0.10, stoichiometric precursors as 1.8475 g CH_3COOLi , 3.4893 g $\text{Ni}_2(\text{NO}_3)_2\cdot 6\text{H}_2\text{O}$, 0.3195 g TiO_2 and 0.3531 g $(\text{NH}_4)_6\text{Mo}_7\text{O}_{24}\cdot 4\text{H}_2\text{O}$ were added into 100 mL distilled water within 3.0 g $\text{C}_6\text{H}_8\text{O}_7\cdot \text{H}_2\text{O}$ (citric acid) as a chelating agent and kept stirring overnight, providing the previous reagent was dissolved completely. The liquid system was first heated at 300 °C for 3 h to evaporate the solvent components. The resulting solid materials were ground into powders in a quartz mortar followed by a calcination process in a furnace under air atmosphere. The calcination step was conducted over 6 h at 750 °C and 800 °C, respectively.

2.2. Electrochemistry

The synthesized active material, carbon black (Super P C65) and polyvinylidene (PVDF) were mixed by a 70:20:10 weight ratio in *N*-methyl-2-pyrrolidone (NMP) and milled in a planetary ball milling machine (Thinky). The obtained slurry was coated on an aluminum foil with a coating doctor blade then dried in a vacuum oven under 90 °C overnight. To assemble coin cells for later electrochemistry tests, lithium foil, Celgard and 1 M of lithium hexafluoride phosphate (LiPF_6) in a mixture of ethylene carbonate and dimethylcarbonate (EC:DMC, 1:1 volume ratio) were used as the counter electrode, the separator, and the electrolyte, respectively. All the electrochemistry performances were measured on the Arbin battery test instrument at room temperature. The specific capacity was calculated based on the actual amount (70%) of active materials in the cathodes.

2.3. Characterizations

Inductively coupled plasma optical emission spectrometer (ICP-OES) was used for the elemental analysis of these synthesized materials via Perkin Elmer Optima 8300. The powder X-ray diffraction patterns of as-prepared samples were collected from a Rigaku D/Max Ultima II Powder with $\text{Cu-K}\alpha$ radiation ($\lambda = 1.54 \text{ \AA}$). The morphology of the synthesized materials was investigated via an FEI Quanta 400 scanning electron microscope and a JEOL 2100F transmission electron microscope (TEM). The oxidation states of transition metals and oxygen ions were obtained by a PHI Quantera X-ray photoelectron spectroscopy (XPS) with Al KR X-ray excitation source of 1.487 keV. In order to study

Table 1

Composition of the electrode materials synthesized in this work, based on ICP-OES analysis.

Sample	Theoretical molar content of Li:Ni:Ti:Mo	Experimental molar content of Li:Ni:Ti:Mo
$\text{Li}_{1.14}\text{Ni}_{0.57}\text{Ti}_{0.19}\text{Mo}_{0.10}\text{O}_2$	1.14:0.57:0.19:0.10	1.126:0.581:0.193:0.100

the oxidation states of different elements for the first charged (4.6 V) and discharged (1.5 V) voltage in the cathode materials, the corresponding tested coin cells were disassembled in the Ar-filled glove box. The reacted electrodes were washed with DMC then dried for 12 h in the glass vials before conducting XPS measurement. Soft X-ray absorption spectra (XAS) were acquired using a 55° incidence angle (magic angle) at the Stanford Synchrotron Radiation Laboratory beamline 8–2 analogous to Ref [14]. The X-ray spot size on the sample position was $< 1 \times 1 \text{ mm}^2$, which allowed scanning several positions sample surface and test for inhomogeneities. The monochromator grating with 1100 1/mm was calibrated by measuring the L_3 edge of a Ni reference in first and second refraction order and setting the energies of the main peaks to 852.7 eV and 426.35 eV, respectively. The TFY XAS spectra were collected under ultrahigh vacuum conditions (10^{-9} Torr) with a silicon photodiode.

3. Results and discussion

According to elemental analysis by ICP-OES technique, the real composition of the materials prepared in this work was found very close to the targeted formula, as tabulated in Table 1. Fig. 1 shows the XRD patterns of samples synthesized under different temperatures. Indeed, the peaks of 2θ values at 37.63°, 43.82°, 63.89°, 76.74° and 80.32° belong to (111), (200), (220), (311) and (222) planes of disordered $\text{LiNi}_{0.5}\text{Ti}_{0.5}\text{O}_2\text{-(Li}_4\text{MoO}_5\text{)}_{0.8}$ (ICDD 00-055-0941, ICDD 01-074-6446), respectively. Therefore, both the patterns have rock-salt disordered phases of $\text{LiNi}_{0.5}\text{Ti}_{0.5}\text{O}_2\text{-(Li}_4\text{MoO}_5\text{)}_{0.8}$. Meanwhile, the prepared material at 800 °C exhibits additional peaks at 18.58°, 36.30°, 37.63°, 44.14°, 48.22°, 58.24°, 64.06°, 67.64°, 77.06° and 81.03° assigned to (003), (101), (006), (104), (015), (107), (018), (113), (021) and (024) planes of LiNiO_2 (ICDD 01-083-9893), respectively. This sample hereafter referred as NTM800. For sample annealed at 750 °C, the reflection peaks corresponding to LiNiO_2 are disappeared, which indicates its transformation into a new phase as $\text{Li}_{0.5}\text{Ni}_{0.5}\text{O}$ (ICDD 04-007-6739) and is denoted as NTM750. Rietveld analysis (Fig. S1, Table S1) by Maud program has been employed on the collected X-ray powder diffraction

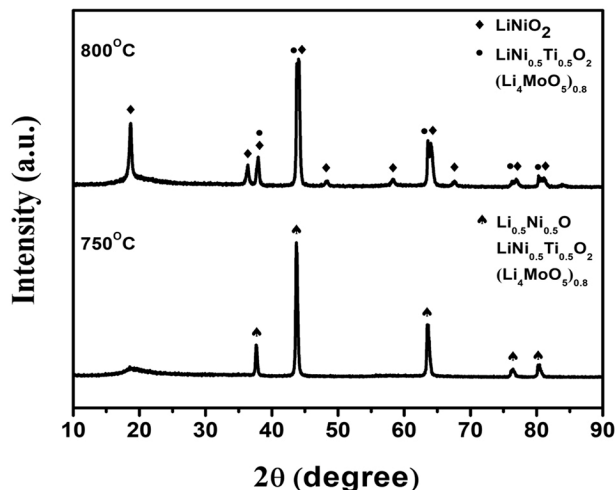


Fig. 1. X-ray diffraction patterns of NTM800, NTM750 annealed at 800 °C, 750 °C for 6 h, respectively.

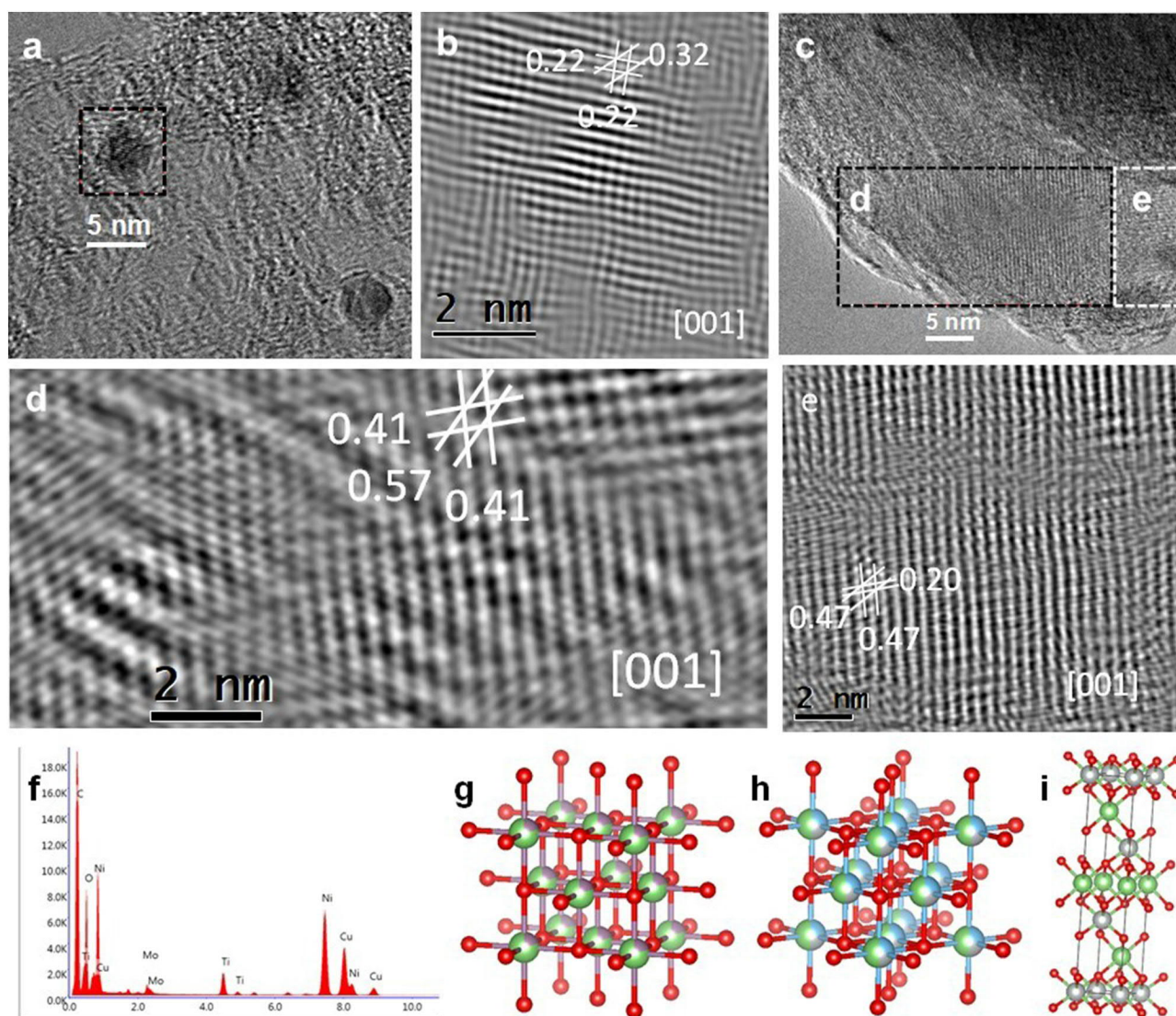


Fig. 2. Transmission electron microscope images of NTM800: (a), (b) $(\text{Li}_4\text{MoO}_5)_{0.8}$ particles along the [001] zone axis; (c), (d) $\text{LiNi}_{0.5}\text{Ti}_{0.5}\text{O}_2$ particles along the [001] zone axis; (e) LiNiO_2 particles along the [001] zone axis; Energy dispersive spectroscopy of NTM800: (f); Crystal structures of identified phases: (g) cubic $(\text{Li}_4\text{MoO}_5)_{0.8}$; (h) cubic $\text{LiNi}_{0.5}\text{Ti}_{0.5}\text{O}_2$; (i) rhombohedral LiNiO_2 .

data of NTM800 for phases analysis, the results show 32.7 wt% $\text{LiNi}_{0.5}\text{Ti}_{0.5}\text{O}_2$ (Fm-3m), 28.0 wt% $(\text{Li}_4\text{MoO}_5)_{0.8}$ (Fm-3m) and 39.3 wt% LiNiO_2 (R-3m), respectively.

Transmission electron microscope (TEM) is used to confirm the characteristic phases of NTM800 inferred from XRD. Fig. 2a–e identify the formation of crystallized $(\text{Li}_4\text{MoO}_5)_{0.8}$, $\text{LiNi}_{0.5}\text{Ti}_{0.5}\text{O}_2$ and LiNiO_2 phases evidenced by the corresponding d-spacing along the [001] zone axis. Moreover, the existence of Ni, Ti, and Mo elements is supported by EDS in Fig. 2f. Finally, Fig. 2g, h, i represents the crystal structure of Fm-3m $(\text{Li}_4\text{MoO}_5)_{0.8}$, Fm-3m $\text{LiNi}_{0.5}\text{Ti}_{0.5}\text{O}_2$ and R-3m LiNiO_2 , respectively. Using TEM, it is possible to recognize the independent domains belonging to the phases mentioned above. For instance, the $(\text{Li}_4\text{MoO}_5)_{0.8}$ has a round-like morphology with approximately 5 nm in size. The characteristic d-spacing (0.22 and 0.32 nm) for this phase correspond to the (200) and (110) planes respectively. On the other hand, the $\text{LiNi}_{0.5}\text{Ti}_{0.5}\text{O}_2$ and LiNiO_2 appear as cluster particles. Their different d-spacing and characteristic planes allow assigning the right stoichiometry to each phase. The $\text{LiNi}_{0.5}\text{Ti}_{0.5}\text{O}_2$ shows d-spacing of 0.41 and 0.57 nm that are typical of the (100) and (110) planes. While for LiNiO_2 the identified planes have d-spacing of 0.47 and 0.20 nm corresponding to the (003) and (102) families. Scanning electron

microscope (SEM, Fig. S2) images of the mixture phases for NTM800 and NTM750 have different morphological features. NTM800 has mainly bulk particles whose diameter is nearly 1 μm . As for NTM750, slightly larger particles with 5 μm diameter agglomerate and form condensed materials. Moreover, the energy-dispersive X-ray spectroscopy (EDS, Fig. S3 and Fig. S4) illustrates the distribution of transitional metal ions in the samples. In Fig. S5, the TEM/EDS shows the high homogeneity of the entire sample, which prevents a precise identification of each phase. However, all the elements present are detected. The EDS results are over-imposed on the high-angle annular dark-field scanning transmission electron microscopy image to discern any potential Z-contrast and compared to chemical composition.

The electrochemical performances of the cathode materials are tested using galvanostatic cycling at a current density of 20 mA/g as depicted in Fig. 3a–c. For NTM800 shown in Fig. 3a, the first charged capacity reaches 194 mAh/g which comprises the oxidation of Ni^{2+} to $\text{Ni}^{3+}/\text{Ni}^{4+}$ and oxygen oxidation process. Upon discharging, the reduction of O^{tr} species is followed by that of Ni^{4+} at higher potentials (> 3.4 V) [24], then the plateau at 1.7 V corresponds to the further reduction of Ni^{3+} to Ni^{2+} [25]. There are approximately 0.21 Ni + 2 and 0.36 Ni + 3 in the as prepared material. The 1.5 V discharge

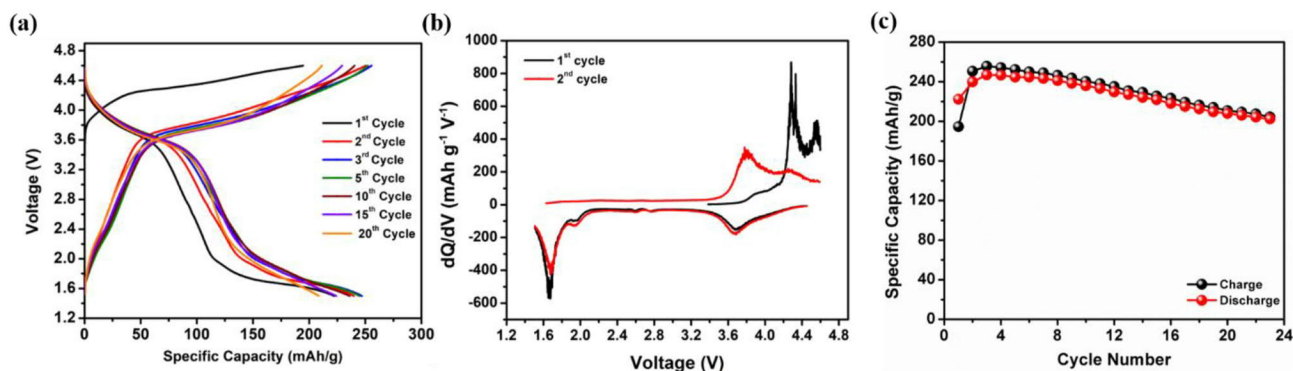


Fig. 3. (a) Galvanostatic charge/discharge profiles of NTM800 under 20 mA/g, (b) dQ/dV versus voltage curves for the first and second cycles of NTM800, (c) Specific capacity versus cycle number of NTM800 under 20 mA/g.

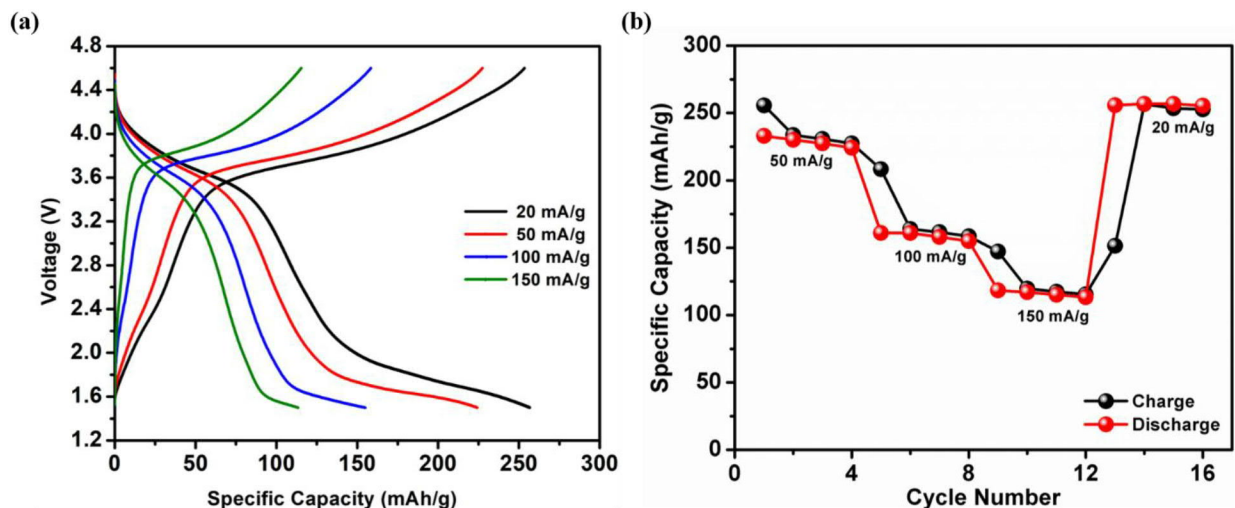


Fig. 4. (a) Voltage profiles of NTM800 when charged and discharged at 20 mA/g, 50 mA/g, 100 mA/g and 150 mA/g, individually for 4 cycles. (b) Specific capacity of NTM800 at 20 mA/g, 50 mA/g, 100 mA/g, 150 mA/g and repeated 20 mA/g, each step contains 4 cycles.

voltage is sufficient to reduce Ni^{3+} to Ni^{2+} and that's the reason that Coulombic Efficiency is observed to be larger than 100% for the first cycle. With the careful observations on derivative curves (Fig. 3b), there are distinctive peaks during first cycle corresponding to nickel and oxygen redox activities. For instance, in the first cycle, oxygen oxidation reaction forms peroxy-like species $O^{•-}$ at above 4.5 V and the oxidation of nickel occurs around 4.3 V. The oxidation peaks of the second cycle both shift to lower potentials indicating the faster kinetics benefiting from the previous activation process. Fig. 3c shows the plot of specific capacity versus cycle numbers for NTM800. After 20 cycles, the capacity of the cathode remains 208 mAh/g that is 94.5% of the initial value of 220 mAh/g while the capacity retention of the sample synthesized at 750 °C is only 73.8% after the same operating period (Fig. S6). As of now, it is important to note that the disordered based cathode materials have limited cycling stability compared to conventional layered cathodes [21]. Given that both cathodes nearly have the same first discharge capacity, the NTM800 cathode has better electrochemical performances. Further, the NTM800 cathode was subjected to several current densities (20-150 mA/g) as plotted in Fig. 4a, b. The cathode delivers a high capacity of 235 mAh/g at 50 mA/g and retains > 100 mAh/g at a high current density of 150 mA/g according to Fig. 4a. As shown in Fig. 4b, the cell is continuously tested at low-current density, and the resulting capacity is still beyond 240 mAh/g. Therefore, the performance of capacity under different current densities demonstrates the reversibility of the structural changes and the oxygen redox reaction in NTM800.

To reveal the underlying electrochemical redox reactions, X-ray

photoelectron spectroscopy (XPS) studies were carried out on the pristine, first charged and first discharged electrodes. Fig. 5a-d represents the XPS of Ni 2p, Ti 2p, Mo 3d and O 1s in NTM800, respectively. In Ni 2p (Fig. 5a) spectra, two peaks at 853.6 eV and 870.9 eV are typical peak positions of $Ni^{2+} \sim 2p_{3/2}$ and $Ni^{2+} \sim 2p_{1/2}$ in nickel oxide materials, respectively [26], accompanied by the $Ni^{3+} \sim 2p_{3/2}$ peak at 856.1 eV [27]. The charged spectrum displays a broader peak at 856.1 eV and an additional characterized peak of Ni^{3+} at 850.0 eV. Such broadening behavior at 856.1 eV peak indicates the formation of Ni^{4+} species [28]. Thus, Ni^{2+} ions are oxidized to Ni^{3+}/Ni^{4+} in the first charge step. Moreover, in a discharged state, the spectrum has the same features of the pristine, which demonstrates the reversible reduction of Ni^{3+}/Ni^{4+} to Ni^{2+} . The electrochemical inactivity of Ti and Mo in the NTM800 cathode (Fig. 5b, c) is understood by XPS and thus these phases stabilize the Ni redox couples. As to oxygen 1s spectra, the peak near 528.0 eV (Fig. 5d) is corresponding to oxygen bonded to lithium although experiencing little shifts when the cell is charged to 4.6 V and then discharged back to 1.5 V [29]. Another peak at 530.9 eV is denoted as the oxygenated deposited species such as Li_2CO_3 at the surface. The new component peak appears at 528.7 eV in the charged part is attributed to the peroxy-like species, i.e., $O^{•-}$ [30], which confirms that oxygen oxidation is occurred during the charging process to deliver extra capacity. In the discharged spectrum, the $O^{•-}$ peak shrinks to a very low intensity compared to that of O^{2-} . Therefore, at least large parts of those peroxy species are reversibly reduced back to O^{2-} . Interestingly, the profile of Ni spectra of NTM750 remains $Ni^{2+/3+}$ after charging to 4.6 V and surprisingly show Ni^{4+} once discharged to

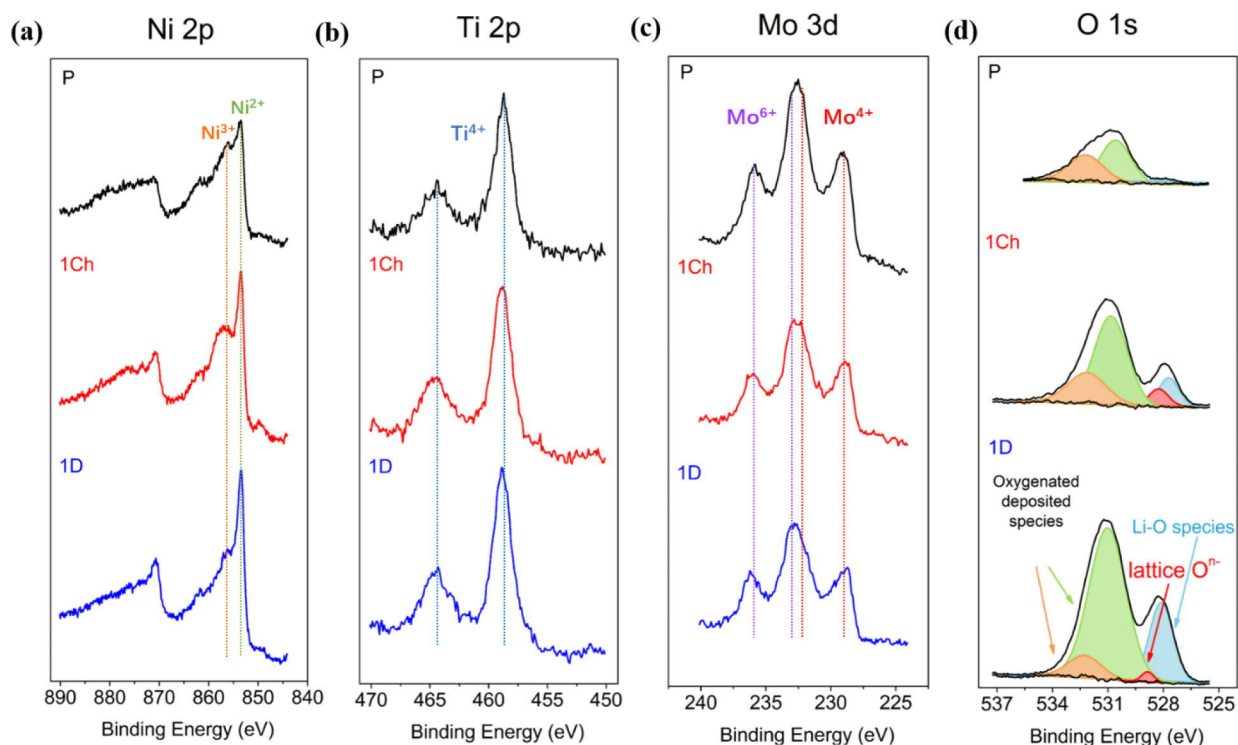


Fig. 5. X-ray photoelectron spectroscopy of the pristine, first charged and first discharged NTM800 electrodes: (a) nickel 2p, (b) titanium 2p, (c) molybdenum 3d, (d) oxygen 1s.

1.5 V. This may be explained by the “metal-driven reductive coupling mechanism” proposed by M. Saubane’re et al. [15] (Fig. S7).

Considering the typical probe depth of low energy XPS (1.487 keV) is around 6 nm that is certainly a surface analysis of elemental chemistry, we conduct soft XAS of NTM800 in TFY mode with ~ 100 nm depth to reveal the chemical behavior of Ni ions in the relative bulk lattice region. Fig. 6a is the spectra of the Ni element in five different states within L_3 -edge (845–857 eV). As previous literature mentioned,

the L_2 -edge (867–875 eV) profile has much broader absorption features suffered from the shorter lifetime of $2p_{1/2}$ core hole as a consequence of Coster-Kronig Auger decay [31], making it difficult to interpret accurate information from this edge. Therefore, Fig. 6a does not involve the L_2 -edge part and the below discussion is focused on L_3 -edge absorption spectra. In the pristine electrode, the main peak at 852.4 eV with a shoulder at 854.4 eV is assigned to Ni^{2+} , accompanied by the characteristic peak of Ni^{3+} at 853.6 eV. This observation is consistent with

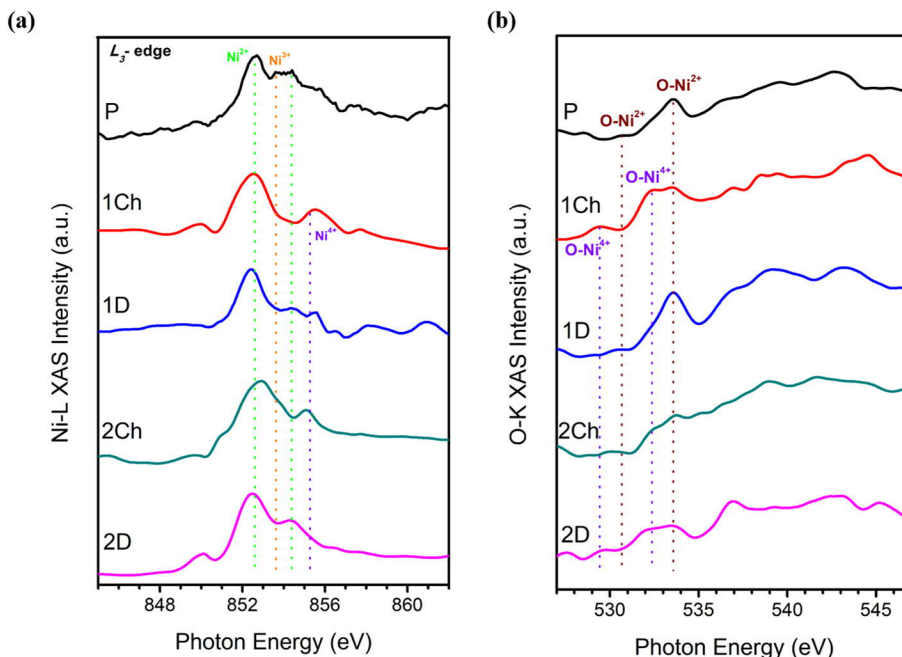


Fig. 6. Soft X-ray absorption spectroscopy of the pristine, first charged, first discharged, second charged and second discharged NTM800 electrodes: (a) nickel-L edge, (b) oxygen-K edge.

our phase identifications of LiNiO_2 and $\text{LiNi}_{0.5}\text{Ti}_{0.5}\text{O}_2$ where Ni shows +2 and +3 valence simultaneously. Once the first charge process completed, the evolved spectra displays a new peak at 855.1 eV attributed to Ni^{4+} . Clearly, parts of Ni^{2+} and all Ni^{3+} have been oxidized into Ni^{4+} while the rest part of Ni^{2+} remains inactive, which indicates the incomplete use of Ni redox reservoir and possible participation of oxygen oxidation to compensate the delivered high capacity. The profile comes back to the pure Ni^{2+} shape line after discharged to 1.5 V in the first cycle, suggesting the good reversibility of cationic redox in the first cycle. The spectra of fully charged and discharged states of the second cycle are recorded as well. As expected, the Ni ions experience the same reaction route as partially being oxidized to Ni^{4+} in charging step then reduced back to Ni^{2+} when it comes to discharging. It should be noted here that all the characteristic peaks of different valences of Ni ions show an energy shift of 1.2 eV compared to standard spectra from literature [31].

It is universally accepted that O K-edge absorption spectra are strongly linked to the hybridization between transition metal (TM) 3d/4d and oxygen 2p orbitals. Therefore, the soft XAS spectra of O K-edge shown in Fig. 6b serve as the proof of the existence of different valences of Ni ions bounded to oxygen ion in different electrochemical test stages. Specifically, the pre-edge peaks between 525 and 535 eV and a broader peak above 535 eV corresponds to hybridization of TM 3d/4d-O 2p and TM 4sp/5sp-O 2p, respectively [14]. A pair of peaks at 533.5 eV and 530.6 eV in the pristine material belong to the excitation process of oxygen 1s core level electron to the orbital hybridized from $\text{Ni}^{2+} d(e_g)\text{-O } 2p$ and $\text{Ni}^{2+} d(t_{2g})\text{-O } 2p$, accordingly. As the first charged spectrum obviously shows an additional couple of peaks at 532.4 eV and 529.4 eV characterized by transition between O 1s and $\text{Ni}^{4+} d\text{-O } 2p$, the formation of Ni^{4+} is confirmed once again. The following first discharged profile has the exact same feature as that of pristine material, as a result, the reduction product of Ni^{2+} dominates the population of Ni valence. Although the general line shape of the second charged profile is similar to that of the first charged one, the ratio of relative intensity of O- Ni^{4+} at 532.4 eV to O- Ni^{2+} at 533.5 eV is decreasing, which may be interpreted as the lower quantity of Ni^{2+} oxidized to Ni^{4+} due to sluggish kinetics or transformation into inactive Ni^{2+} species. Noticeably, the relative intensity of O- Ni^{4+} does not drop at the end of second discharged state. One may explain the phenomena on account of partial irreversible Ni^{4+} in the second electrochemical cycle. Here, we decide not to analyze the redox reaction between O^{2-} and $\text{O}^{\cdot-}$ solely based on soft XAS of O K-edge. Indeed, researchers have recognized the difficulty to analyze the hybridization peaks and O 2p states independently owing to their highly overlapping features. Moreover, whether the oxygen redox happens or not, the intensity of the pre-edge will definitely increase upon charging since Li removal leads to more covalent nature between TM and O, thus enhancing the TM-O hybridization.

Fig. 7 shows high-resolution TEM (HRTEM) analysis for the NTM800 of the discharged samples after one cycle, and 20 cycles and they are compared to the pristine material. Based on the XPS results (Fig. 5c), Mo does not seem to contribute or change drastically in the process. Therefore, one may expect limited changes in the Mo-rich phase. In the first cycle, it is clear that $(\text{Li}_4\text{MoO}_5)_{0.8}$ does not present noticeable changes in microstructure, size or morphology (Fig. 7b) while the LiNiO_2 (Fig. 7c) and $\text{LiNi}_{0.5}\text{Ti}_{0.5}\text{O}_2$ (Fig. 7e) phases present appreciable changes in the lattice that is perceived as distortion. The LiNiO_2 and $\text{LiNi}_{0.5}\text{Ti}_{0.5}\text{O}_2$ phases transformed from a 10–20 nm short-range structure into a distorted lattice that looks like a series of dislocations forming short-range order particles. It is of further interest to recognize that after 20 cycles, the $(\text{Li}_4\text{MoO}_5)_{0.8}$ phase does not report changes as observed from Fig. 7g. At the same time, the $\text{LiNi}_{0.5}\text{Ti}_{0.5}\text{O}_2$ (Fig. 7h) and LiNiO_2 (Fig. 7i) phases change from nanostructure (10–20 nm, see Fig. 2) into 1–2 nm domains with wide grain boundaries and distorted planes. The HRTEM results confirm the limited electrochemical contribution of the $(\text{Li}_4\text{MoO}_5)_{0.8}$ phase and the high

homogeneity of the investigated samples (Fig. 7a, f, Fig. S8 and Fig. S9).

4. Conclusions

In conclusion, we synthesized the Li/Ni-rich Ni-Ti-Mo oxide cathodes using citric acid-assisted solution method. The detailed phase analysis of prepared materials is performed by X-ray diffraction and transmission microscopy, revealing the formation of mixed phases such as $(\text{Li}_4\text{MoO}_5)_{0.8}$, $\text{LiNi}_{0.5}\text{Ti}_{0.5}\text{O}_2$ and LiNiO_2 at 800 °C. For this cathode material, partially reversible oxygen redox reaction, i.e., the transformation between O^{2-} and $\text{O}^{\cdot-}$, contributes to the total capacity during charging and discharging processes. The NTM800 cathode exhibiting $\text{Ni}^{2+} \sim \text{Ni}^{3+}/\text{Ni}^{4+}$ redox reaction along with capacity from anion contribution enables better electrochemical performances. Although the reductive coupling mechanism is triggered in the NTM750 cathode, it is not effective enough to stabilize the formed peroxy species that inevitably causes the oxygen loss and the accompanying reduction of molybdenum ions. The specific capacity of NTM800 reaches beyond 240 mAh/g and it shows reasonable high rate performance up to 150 mA/g, which evidences the good reversibility of structural changes. The underlying mechanism is the transformation between Ni^{2+} and Ni^{4+} along with oxygen redox reaction during cycling evidenced by the combination of XPS and soft XAS studies, while the irreversible part of oxygen redox may explain the obvious capacity decay reflected from 94.5% capacity retention of NTM800 after 20 cycles.

The future work will focus on the F doping of Li/Ni rich cathode materials to exploit the $\text{Ni}^{2+}/\text{Ni}^{4+}$ redox reservoir, thus relieving the structural instability due to the involvement of oxygen oxidation. Operando XAS data should be collected and analyzed by Principal Component Analysis (PCA) and Multivariate Curve Resolution-Alternating Least Squares (MCR-ALS) methods first introduced by Tauler et al. to calculate the exact capacity contribution from Ni ions [12,32–35]. Then the oxygen participation is revealed simply via subtracting the part of Ni from the total capacity. The obtained result will be compared to that deduced from the measurement by Differential Electrochemical Mass Spectrometry (DEMS) which is purely attributed to oxygen gas release [36], and the difference is the amount of capacity based on reversible oxygen redox reaction. The accurately quantitative analysis will predict whether oxygen redox reaction is realistic to reach extremely high energy density cathodes for Li-ion batteries.

CRediT authorship contribution statement

Jianan Xu: Investigation, Data curation, Formal analysis, Methodology and Writing - review & editing. **Ganguli Babu:** Conceptualization, Supervision and Writing - review & editing. **Keiko Kato:** Investigation, Formal analysis and Writing - review & editing. **Francisco C. Robles Hernández:** Investigation, Formal analysis and Writing - review & editing. **Anand B. Puthirath:** Investigation, Formal analysis and Writing - review & editing. **Alexander Britz:** Investigation, Software and Writing - review & editing. **Dennis Nordlund:** Writing - review & editing. **Sami Sainio:** Investigation, Software and Writing - review & editing. **Uwe Bergmann:** Investigation, Software and Writing - review & editing. **Pulickel M. Ajayan:** Conceptualization, Supervision and Writing - review & editing.

Declaration of competing interest

The authors declare that they have no known competing financial interests or personal relationships that could have appeared to influence the work reported in this paper.

Acknowledgments

A.B.P. thank the Science and Engineering Research Board (SERB) and Indo-US Science and Technology Forum (IUSSTF) for financial

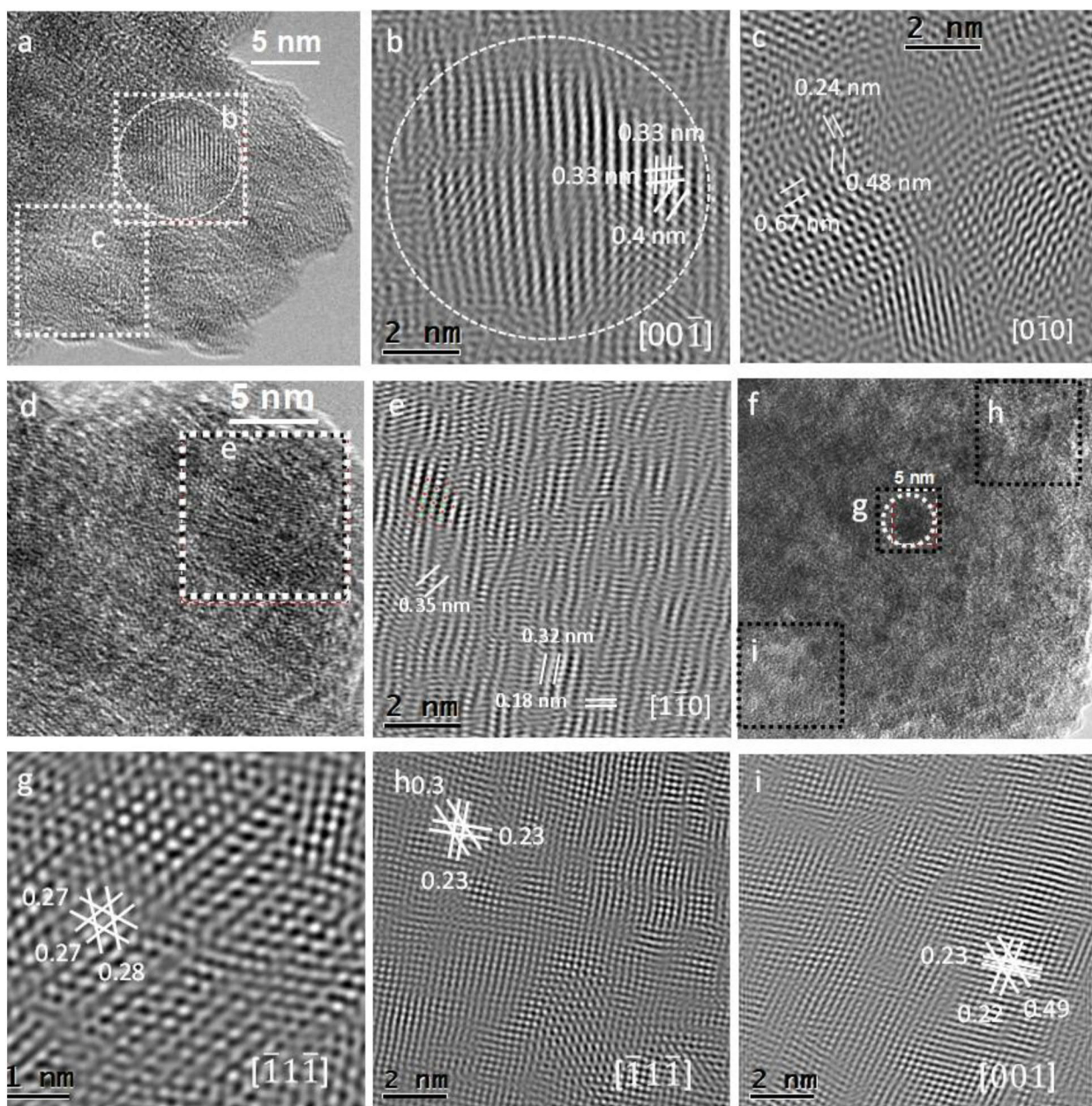


Fig. 7. Transmission electron microscope images of NTM800: after 1 cycle (a–e) and 20 cycles (f–i). In (a) one can observe regions (b, c) that were identified as (b) $(\text{Li}_4\text{MoO}_5)_{0.8}$ and (c) LiNiO_2 . In region (d, e) is presented the $\text{LiNi}_{0.5}\text{Ti}_{0.5}\text{O}_2$. In the samples tested for 20 cycles we can observe the three phases co-existing in a single field as (g) $(\text{Li}_4\text{MoO}_5)_{0.8}$, (h) $\text{LiNi}_{0.5}\text{Ti}_{0.5}\text{O}_2$ and (i) LiNiO_2 .

support in the form of postdoctoral fellowship. A.B. and U.B. where supported by the Computational Materials Sciences Program funded by the U.S. Department of Energy, Office of Science, and Basic Energy Sciences, under Award Number DE-SC00014607. Use of the Stanford Synchrotron Radiation Light source, SLAC National Accelerator Laboratory, is supported by the U.S. Department of Energy, Office of Science, Office of Basic Energy Sciences under Contract No. DE-AC02-76SF00515.

Appendix A. Supplementary data

Supplementary data to this article can be found online at <https://doi.org/10.1016/j.ssi.2019.115172>.

References

- [1] G. Babu, N. Kalaiselvi, D. Bhuvaneshwari, Synthesis and surface modification of $\text{LiCo}_{1/3}\text{Ni}_{1/3}\text{Mn}_{1/3}\text{O}_2$ for lithium battery applications, *J. Electron. Mater.* 43 (2014) 1062–1070.
- [2] R. Lakshmanan, D. Gangulibabu, N. Kalaiselvi Bhuvaneshwari, Temperature dependent surface morphology and lithium diffusion kinetics of LiCoO_2 cathode, *Met. Mater. Int.* 18 (2012) 249–255.
- [3] A. Yamada, S.-C. Chung, K. Hinokuma, Optimized LiFePO_4 for lithium battery cathodes, *J. Electrochem. Soc.* 148 (2001) A224–A229.
- [4] R. Wang, X. Li, L. Liu, J. Lee, D.-H. Seo, S.-H. Bo, A. Urban, G. Ceder, A disordered rock-salt Li-excess cathode material with high capacity and substantial oxygen redox activity: $\text{Li}_{1.25}\text{Nb}_{0.25}\text{Mn}_{0.5}\text{O}_2$, *Electrochem. Commun.* 60 (2015) 70–73.
- [5] X. Wang, W. Huang, S. Tao, H. Xie, C. Wu, Z. Yu, X. Su, J. Qi, Z. Rehman, L. Song, G. Zhang, W. Chu, S. Wei, Attainable high capacity in Li-excess Li-Ni-Ru-O rock-salt cathode for lithium ion battery, *J. Power Sources* 359 (2017) 270–276.
- [6] S. Hoshino, A.M. Glushenkov, S. Ichikawa, T. Ozaki, T. Inamasu, N. Yabuuchi, Reversible three-electron redox reaction of $\text{Mo}^{3+}/\text{Mo}^{6+}$ for rechargeable lithium batteries, *ACS Energy Lett.* 2 (2017) 733–738.
- [7] Q. Jacquet, A. Perez, D. Batuk, G. Van Tendeloo, G. Rousse, J.-M. Tarascon, The

- $\text{Li}_3\text{Ru}_y\text{Nb}_{1-y}\text{O}_4$ ($0 \leq y \leq 1$) system: structural diversity and Li insertion and extraction capabilities, *Chem. Mater.* 29 (2017) 5331–5343.
- [8] B. Li, D. Xia, Anionic redox in rechargeable lithium batteries, *Adv. Mater.* 29 (2017) 1701054.
- [9] E. McCalla, M.T. Sougrati, G. Rousse, E.J. Berg, A. Abakumov, N. Recham, K. Ramesha, M. Sathiya, R. Dominko, G. Van Tendeloo, P. Novak, J.M. Tarascon, Understanding the roles of anionic redox and oxygen release during electrochemical cycling of lithium-rich layered $\text{Li}_4\text{FeSbO}_6$, *J. Am. Chem. Soc.* 137 (2015) 4804–4814.
- [10] K. Luo, M.R. Roberts, R. Hao, N. Guerrini, D.M. Pickup, Y.S. Liu, K. Edstrom, J. Guo, A.V. Chadwick, L.C. Duda, P.G. Bruce, Charge-compensation in 3d-transition-metal-oxide intercalation cathodes through the generation of localized electron holes on oxygen, *Nat. Chem.* 8 (2016) 684–691.
- [11] D.H. Seo, J. Lee, A. Urban, R. Malik, S. Kang, G. Ceder, The structural and chemical origin of the oxygen redox activity in layered and cation-disordered Li-excess cathode materials, *Nat. Chem.* 8 (2016) 692–697.
- [12] G. Assat, A. Iadecola, C. Delacourt, R. Dedryvère, J.-M. Tarascon, Decoupling cationic–anionic redox processes in a model Li-rich cathode via operando X-ray absorption spectroscopy, *Chem. Mater.* 29 (2017) 9714–9724.
- [13] M. Tang, A. Dalzini, X. Li, X. Feng, P.H. Chien, L. Song, Y.Y. Hu, Operando EPR for simultaneous monitoring of anionic and cationic redox processes in Li-rich metal oxide cathodes, *J. Phys. Chem. Lett.* 8 (2017) 4009–4016.
- [14] J. Xu, M. Sun, R. Qiao, S.E. Renfrew, L. Ma, T. Wu, S. Hwang, D. Nordlund, D. Su, K. Amine, J. Lu, B.D. McCloskey, W. Yang, W. Tong, Elucidating anionic oxygen activity in lithium-rich layered oxides, *Nat. Commun.* 9 (2018) 947.
- [15] M. Saubanère, E. McCalla, J.M. Tarascon, M.L. Doublet, The intriguing question of anionic redox in high-energy density cathodes for Li-ion batteries, *Energy Environ. Sci.* 9 (2016) 984–991.
- [16] M. Okubo, A. Yamada, Molecular orbital principles of oxygen-redox battery electrodes, *ACS Appl. Mater. Interfaces* 9 (2017) 36463–36472.
- [17] N. Yabuuchi, M. Nakayama, M. Takeuchi, S. Komaba, Y. Hashimoto, T. Mukai, H. Shiiba, K. Sato, Y. Kobayashi, A. Nakao, M. Yonemura, K. Yamanaka, K. Mitsuhashi, T. Ohta, Origin of stabilization and destabilization in solid-state redox reaction of oxide ions for lithium-ion batteries, *Nat. Commun.* 7 (2016) 13814.
- [18] Y. Zuo, B. Li, N. Jiang, W. Chu, H. Zhang, R. Zou, D. Xia, A high-capacity O_2 -type Li-rich cathode material with a single-layer Li_2MnO_3 superstructure, *Adv. Mater.* 30 (2018) e1707255.
- [19] A.J. Perez, Q. Jacquet, D. Batuk, A. Iadecola, M. Saubanère, G. Rousse, D. Larcher, H. Vezin, M.-L. Doublet, J.-M. Tarascon, Approaching the limits of cationic and anionic electrochemical activity with the Li-rich layered rocksalt Li_3IrO_4 , *Nat. Energy* 2 (2017) 954–962.
- [20] J. Lee, D.-H. Seo, M. Balasubramanian, N. Twu, X. Li, G. Ceder, A new class of high capacity cation-disordered oxides for rechargeable lithium batteries: Li–Ni–Ti–Mo oxides, *Energy Environ. Sci.* 8 (2015) 3255–3265.
- [21] J. Lee, J.K. Papp, R.J. Clement, S. Sallis, D.H. Kwon, T. Shi, W. Yang, B.D. McCloskey, G. Ceder, Mitigating oxygen loss to improve the cycling performance of high capacity cation-disordered cathode materials, *Nat. Commun.* 8 (2017) 981.
- [22] M. Sathiya, A.M. Abakumov, D. Foix, G. Rousse, K. Ramesha, M. Saubanere, M.L. Doublet, H. Vezin, C.P. Laisa, A.S. Prakash, D. Gonbeau, G. VanTendeloo, J.M. Tarascon, Origin of voltage decay in high-capacity layered oxide electrodes, *Nat. Mater.* 14 (2015) 230–238.
- [23] J. Lee, A. Urban, X. Li, D. Su, G. Hautier, G. Ceder, Unlocking the potential of cation-disordered oxides for rechargeable lithium batteries, *Science* 343 (2014) 519–522.
- [24] C.H. Shen, Q. Wang, F. Fu, L. Huang, Z. Lin, S.Y. Shen, H. Su, X.M. Zheng, B.B. Xu, J.T. Li, S.G. Sun, Facile synthesis of the Li-rich layered oxide $\text{Li}_{1.23}\text{Ni}_{0.09}\text{Co}_{0.12}\text{Mn}_{0.56}\text{O}_2$ with superior lithium storage performance and new insights into structural transformation of the layered oxide material during charge-discharge cycle: in situ XRD characterization, *ACS Appl. Mater. Interfaces* 6 (2014) 5516–5524.
- [25] L. Zhang, H. Noguchi, D. Li, T. Muta, X. Wang, M. Yoshio, I. Taniguchi, Synthesis and electrochemistry of cubic rocksalt Li–Ni–Ti–O compounds in the phase diagram of LiNiO_2 – LiTiO_2 – $\text{Li}[\text{Li}_{1/3}\text{Ti}_{2/3}]\text{O}_2$, *J. Power Sources* 185 (2008) 534–541.
- [26] A.N. Mansour, Characterization of NiO by XPS, *Surf. Sci. Spectra* 3 (1994) 231–238.
- [27] A.N. Mansour, Characterization of LiNiO_2 by XPS, *Surf. Sci. Spectra* 3 (1994) 279–286.
- [28] K.J. Carroll, D. Qian, C. Fell, S. Calvin, G.M. Veith, M. Chi, L. Baggetto, Y.S. Meng, Probing the electrode/electrolyte interface in the lithium excess layered oxide $\text{Li}_{1.2}\text{Ni}_{0.2}\text{Mn}_{0.6}\text{O}_2$, *Phys. Chem. Chem. Phys.* 15 (2013) 11128–11138.
- [29] M. Olschewski, R. Gustus, M. Marschewski, O. Hoff, F. Endres, Spectroscopic characterization of the interaction of lithium with thin films of the ionic liquid 1-octyl-3-methylimidazolium bis(trifluoromethylsulfonyl)amide, *Phys. Chem. Chem. Phys.* 16 (2014) 25969–25977.
- [30] D. Foix, M. Sathiya, E. McCalla, J.-M. Tarascon, D. Gonbeau, X-ray photoemission spectroscopy study of cationic and anionic redox processes in high-capacity Li-ion battery layered-oxide electrodes, *J. Phys. Chem. C* 120 (2016) 862–874.
- [31] R. Qiao, L.A. Wray, J.-H. Kim, N.P.W. Pieczonka, S.J. Harris, W. Yang, Direct experimental probe of the Ni(II)/Ni(III)/Ni(IV) redox evolution in $\text{LiNi}_{0.5}\text{Mn}_{1.5}\text{O}_4$ electrodes, *J. Phys. Chem. C* 119 (2015) 27228–27233.
- [32] A. de Juan, R. Tauler, Chemometrics applied to unravel multicomponent processes and mixtures, *Anal. Chim. Acta* 500 (2003) 195–210.
- [33] T. Broux, T. Bamine, L. Simonelli, L. Stievano, F. Fauth, M. Ménétrier, D. Carlier, C. Masquelier, L. Croguennec, V^{IV} disproportionation upon sodium extraction from $\text{Na}_3\text{V}_2(\text{PO}_4)_2\text{F}_3$ observed by operando X-ray absorption spectroscopy and solid-state NMR, *J. Phys. Chem. C* 121 (2017) 4103–4111.
- [34] A. Iadecola, A. Perea, L. Aldon, G. Aquilanti, L. Stievano, Li deinsertion mechanism and Jahn–Teller distortion in $\text{LiFe}_{0.75}\text{Mn}_{0.25}\text{PO}_4$: an operando X-ray absorption spectroscopy investigation, *J. Phys. D. Appl. Phys.* 50 (2017) 144004.
- [35] L.C. Loaiza, E. Salager, N. Louvain, A. Boulaoued, A. Iadecola, P. Johansson, L. Stievano, V. Seznec, L. Monconduit, Understanding the lithiation/delithiation mechanism of $\text{Si}_{1-x}\text{Ge}_x$ alloys, *J. Mater. Chem. A* 5 (2017) 12462–12473.
- [36] K. Luo, M.R. Roberts, N. Guerrini, N. Tapia-Ruiz, R. Hao, F. Massel, D.M. Pickup, S. Ramos, Y.S. Liu, J. Guo, A.V. Chadwick, L.C. Duda, P.G. Bruce, Anion redox chemistry in the cobalt free 3d transition metal oxide intercalation electrode $\text{Li}[\text{Li}_{0.2}\text{Ni}_{0.2}\text{Mn}_{0.6}]\text{O}_2$, *J. Am. Chem. Soc.* 138 (2016) 11211–11218.